Quasicrystal approximants in the two-dimensional Ba-Ti-O system on Pd(111): A LEED, XPS, and STM study

Friederike Elisa Wührl, Oliver Krahn, Sebastian Schenk, Wolf Widdra ⓞ, and Stefan Förster ⓞ[*]

Institute of Physics, Martin-Luther-Universität Halle-Wittenberg, D-06099 Halle, Germany

Long-range aperiodically ordered dodecagonal oxide quasicrystals (OQCs) have been observed on Pt(111), together with a variety of related approximants. All structures contain barium, titanium, and oxygen atoms in Ti_nO_n ring structures with rings of $n = 4$, 7, and 10. Barium decorates the larger rings and forms a dodecagonal square-triangle-rhombus tiling. In contrast to these studies on Pt(111), we report here on Ba-Ti-O layers on Pd(111), which has a 1% smaller lattice constant than Pt(111). We find a series of quasicrystal approximants with unit cells consisting of up to 60 triangles, 22 squares, and eight rhombuses. The latter resembles the largest quasicrystal approximant reported to date. The basis for these structures are local patches of the σ-phase square-triangle approximant, into which rhombuses are incorporated due to the formation of ordered antiphase domain boundaries in two orthogonal directions. A structural phase diagram of all quasicrystal approximants on Pd(111) system is presented.

I. INTRODUCTION

The dodecagonal oxide quasicrystals (OQCs), which form on hexagonal close-packed metal substrates, are a unique model systems to address the peculiar properties of quasicrystalline systems and aperiodic order. Due to their truly two-dimensional character they provide full access to structural details on the atomic scale by the tools of surface science. OQCs emerge in ultrathin Ba-Ti-O and Sr-Ti-O layers on Pt(111) [1–3]. A Ti_nO_n network structure with ring sizes of $n = 4$, 7, and 10 forms the backbone of the OQCs and of the related periodic approximants as has been proposed earlier by Cockayne *et al.* and experimentally verified only recently [4,5]. While the smallest $n = 4$ rings of the network remain empty, $n = 7$ rings are decorated by one alkaline earth metal atom (Ba or Sr) and $n = 10$ rings contain two alkaline earth metal atoms [4,5]. By connecting all alkaline earth metal atoms, square-triangle-rhombus tilings are formed. It is the first natural representation of the mathematical Niizeki-Gähler square-triangle-rhombus tiling (NGT) [6–8]. On Pt(111), the aperiodic OQC is the dominant structure for a Ba atom density of $2.46/nm^2$, whereas other densities lead to periodic approximants [4,9–16].

But why do ternary oxide films spontaneously form aperiodic structures? The different quality of the long-range aperiodic order in the Ba-Ti-O/Pt(111) and Sr-Ti-O/Pt(111) systems indicate that the lattice mismatch between the parent ternary oxide and the metal support plays a crucial role for the stabilization of dodecagonal oxide layers. While for Ba-Ti-O/Pt(111) the aperiodic long-range ordering is perfect [3,8], periodic approximant phases are preferred above the OQC formation in Sr-Ti-O/Pt(111) [2,5,15]. When looking

to the parent bulk materials, the lattice mismatch between $BaTiO_3$ and Pt(111) amounts to –2% . In contrast, $SrTiO_3$ and Pt(111) have matching lattice parameters, which seems not to be beneficial for promoting the dodecagonal structure. For imposing a larger lattice mismatch of –4.5%, Ba-Ti-O films have been grown on Ru(0001). However also for this materials combination a commensurate square-triangle tiling known as σ-phase approximant or $3^2.4.3.4$ Archimedean tiling is epitaxially stabilized [12].

Here we report on complex square-triangle-rhombus tilings formed in Ba-Ti-O on Pd(111). For this materials combination a nominal lattice mismatch of –2.8% can be calculated, close to the conditions in $BaTiO_3$/Pt(111). Upon annealing in ultrahigh vacuum (UHV) at 930 K to 1030 K, reduced Ba-Ti-O forms long-range ordered two-dimensional layers on the Pd substrate. In these wetting layers, a series of structures is identified by means of scanning tunneling microscopy (STM) and low-energy electron diffraction (LEED). Previously, small unit-cell approximants consisting of four Ba atoms per unit cell have been reported [16]. In this paper we focus on complex tilings obtained for a Ba vertex density compatible with the OQC structure.

Finally by applying the approved structural model, all observed structures are contextualized in a structural phase diagram of the Ba-Ti-O/Pd(111) system.

II. METHODS

Sample growth, LEED, and x-ray photoelectron spectroscopy (XPS) experiments have been carried out in an UHV system operating at a base pressure of 1×10^{-10} mbar. Pd(111) substrates (Mateck, Germany) were cleaned by repeated cycles of Ar^+ ion sputtering at 1 keV and a two-step annealing process. After annealing the crystal briefly at 1170 K for 30 s to heal out sputter-induced surface
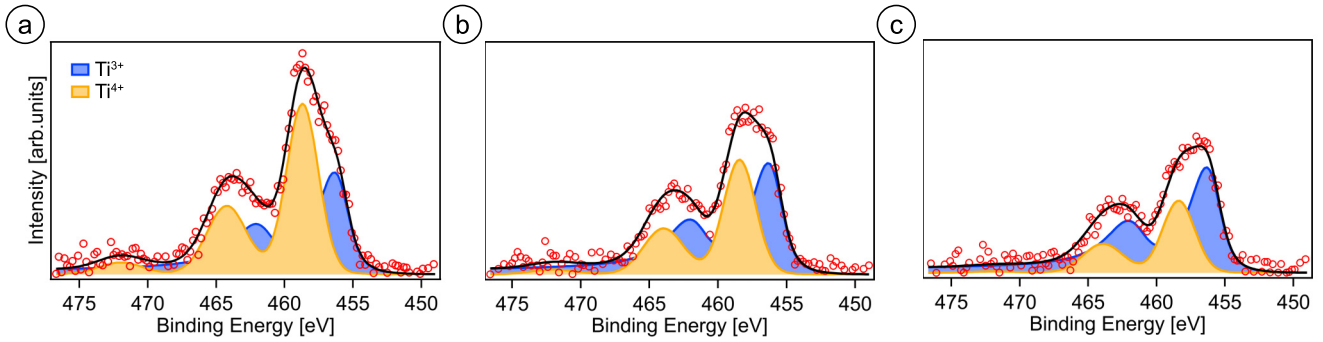
*stefan.foerster@physik.uni-halle.de

FIG. 1. Ti2*p* XPS spectra for ultrathin Ba-Ti-O on Pd(111) upon long-term UHV annealing at 940 K. By varying the thickness of the deposited film from (a) 7.1 Å to (b) 5.6 Å and (c) 5.4 Å, the Ti^{4+}:Ti^{3+} peak area ratio changes from 4:3 to 1:2.

roughening, the crystal was kept at 900 K for 10 min at an oxygen partial pressure of 1×10^{-6} mbar. During the second step, residual carbon contaminations are oxidized to CO, which immediately desorbs at high temperatures. Due to the low sticking probability of oxygen on palladium at elevated temperatures, a clean metal surface is obtained. Temperatures have been monitored using a pyrometer at an emissivity of 0.17 (Pyrospot DG40N, DIAS, $\lambda = 1600$ nm). Ba was supplied from a commercial Ba dispenser source (SAES Getters). Ti was evaporated from a rod. Film thickness is estimated using a quartz crystal microbalance maintained at 345 K. Metal layers were deposited at room temperature and postoxidized by annealing in an oxygen atmosphere of 1×10^{-5} mbar for 20 min at 770 K. The XPS measurements were performed using nonmonochromatized Al-Kα excitation. For detection a 127° analyzer equipped with a single channeltron was used. From the measured data, Al-Kα satellites, an experimentally determined background of the bare substrate, and an additional Shirley background were subtracted prior to fitting. The XPS binding energy axis was calibrated to a Pd3d$_{5/2}$ core level energy of 335.2 eV [17]. The STM measurements were performed in a home-built STM. All measurements presented here were conducted at liquid nitrogen temperatures and in constant current regime.

Custom code was used for LEED pattern calculation using point-like atoms under kinematic scattering with atomic form factor set to unity for all atoms, similar to earlier paper [2]. For these calculations only the Ba atoms that scatter electrons the most have been considered. Calculated single domain patterns were further duplicated, symmetrically rotated, and mirrored according to the substrate symmetry. To compare the calculated pattern with experiment, the calculated intensities were plotted as 2D Gaussian profiles.

III. RESULTS

Ba-Ti-O films of different thickness have been prepared by sequential evaporation of Ba and Ti onto Pd(111) at room temperature. As read from the quartz-crystal microbalance (QMB) nominally 3 Å Ba and 2 Å Ti have been deposited initially, which has later been reduced by 25% and 30%. Upon full oxidation by post annealing at 770 K in 10^{-5} mbar O$_2$, film thickness and composition have been monitored by XPS as described in detail previously [16]. For the three

preparations mentioned above, thicknesses of 7.1, 5.6, and 5.4 Å have been determined, respectively, and a uniform Ba:Ti ratio of 0.5:1. A higher initial Ti content has been chosen intentionally to compensate for Ti segregation into the Pd(111) bulk upon high-temperature annealing [18]. UHV annealing of Ba-Ti-O on Pd(111) results in a phase separation into a two-component oxide system similar to related materials systems [2,12,19]. Bulk-like BaTiO$_3$(111) islands form that tend to dewet the surface while the free Pd(111) area is covered by a two-dimensional oxide layer. This phase separation can be monitored in the Ti2*p* region by XPS. Figure 1 compares the spectra for all three film thicknesses upon prolonged UHV annealing at 940 K. The high binding-energy component corresponds to fully oxidized Ti in bulk-like BaTiO$_3$ islands. The second doublet is found at 2.0 eV lower binding energy, corresponding to Ti in the two-dimensional ternary oxide layer. Figure 1 illustrates that by reducing the overall amount of material during deposition the balance between the two oxide species can be shifted in favor of the 2D component.

Irrespective of the initial film thickness, a long-range ordered hexagonal phase is formed in the 2D layer upon short term UHV annealing at 940 K [16]. Prolonged annealing ($\geqslant 60$ min) at 940 K however, induces complex long-range ordered structure as revealed by LEED. Figures 2(a)–(c) shows the typical electron diffraction pattern recorded at different energies. Twelve pairs of high-intensity spots at about 1.0 Å^{-1} dominate the pattern at all energies. From observing twenty four spots one could speculate about a dodecagonal structure that is rotated against the mirror axis of the hexagonal substrate. In this case, the existence of a mirrored domain would result in a spot doubling. However, a close inspection of these intense spots at the lowest energy shown in Fig. 2(a) reveals a triangular shape. This suggests a partial overlap of three nearby spots at these positions, which points to a large unit-cell approximant phase. Another indication towards a periodic approximant phase is that these most intense spots are neither equally spaced in terms of rotational angles, nor have a constant distance to the origin. This is determined precisely by extracting a thick-line profile centered at 1.05 Å^{-1}. Figure 2(d) shows a cut along 180° through the LEED data taken at 25 eV in the direction of the red arrow. In this representation differences in $|\vec{q}|$ of 0.02 Å^{-1} can be determined for the spots of highest intensity. Please note also the triangular spot splitting at 1.4 Å^{-1}. The large number of low-intensity spots
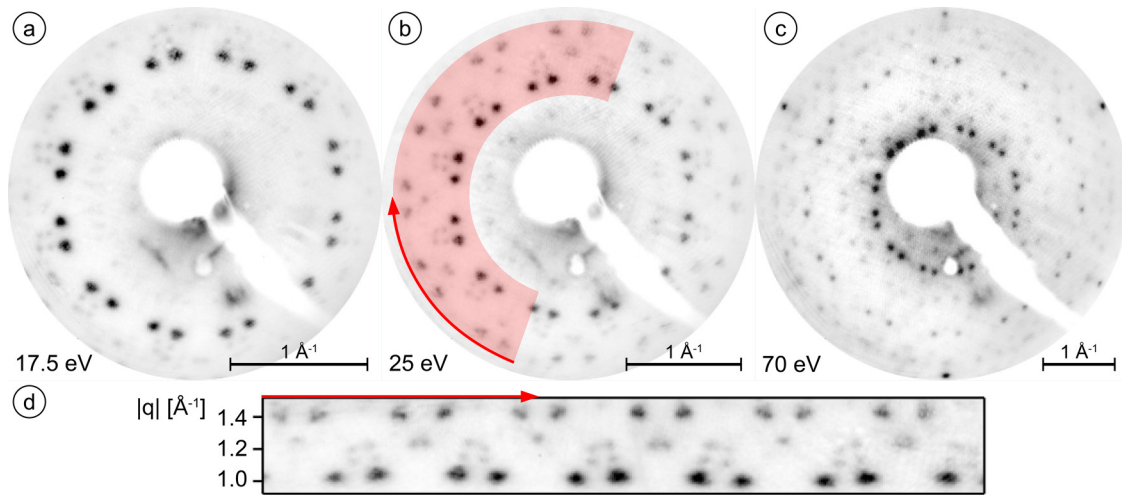
FIG. 2. [(a)–(c)] LEED data of 5.6 Å Ba-Ti-O on Pd(111) upon long-term UHV annealing at 940 K at different kinetic energies as indicated. (d) Line profile taken from (b) in the indicated region in the direction of the red arrow.

in close vicinity is another indication towards existence of a small unit cell in reciprocal space. From this plot, an angular spacing between mirror domain spots of $10.5°$ is obtained.

In STM, the formation of a continuous two-dimensional wetting layer of high structural perfection is observed. Figure 3(a) shows a large area scan in which well-separated protrusions dominate. Sometimes two nearby protrusions are seen as streaks, which occur in two distinct orientations in this image. The inset in Fig. 3(a) shows the Fourier transform of the STM image. It reveals a high aspect-ratio grid with short reciprocal lattice vectors and strong intensity variations. The highest spot intensities are found at about $1.05\,\text{Å}^{-1}$ in correspondence to the prominent spots seen in LEED. From the atomically resolved image the atomic coordinates have

been extracted to obtain the tiling shown in Fig. 3(b). In the tiling of Fig. 3(b) rows of individual rhombuses can be recognized. They appear in a given sequence: two rows of similarly oriented rhombuses are followed by an alternating sequence of rows of $90°$ rotated rhombuses. This helps to identify the unit cell, which is given as an inset in Fig. 3(b). The unit cell of this structure contains 40 vertex atoms. It is now established that the protrusions seen in STM are the Ba atoms [5]. The Ti_nO_n network structure hosting the Ba atoms is not seen in STM. These 40 Ba atoms can be connected to a tiling of 40 triangles, 15 squares, and five rhombuses. Encoding the tiling element frequency, this structure can be called a 40:15:5 approximant. For the sake of simplicity it will be denoted as **5R** approximants throughout this paper.
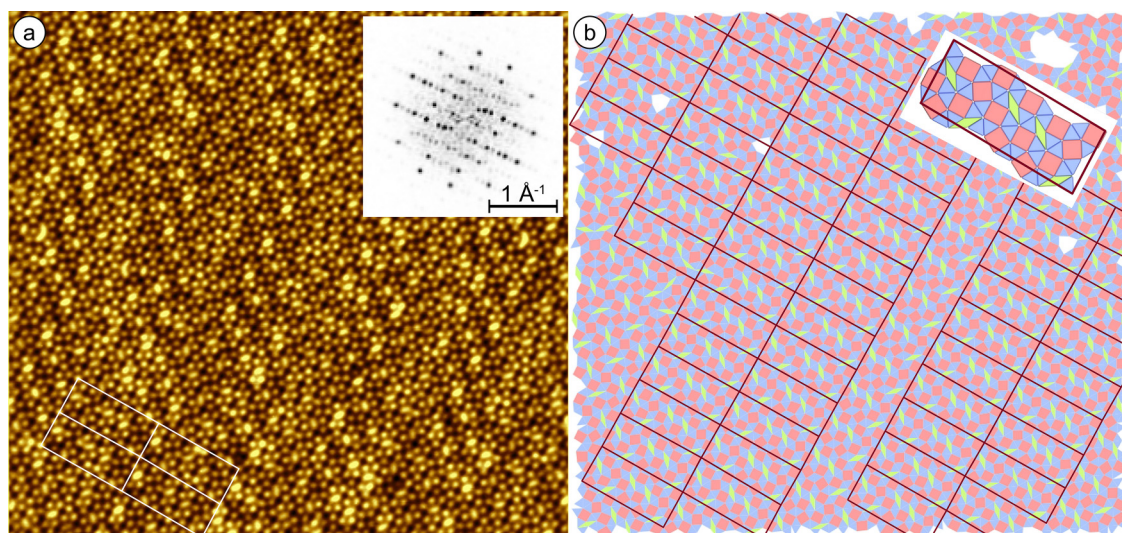

FIG. 3. STM data of 5.6 Å Ba-Ti-O on Pd(111) upon long-term UHV annealing at 940 K. (a) Large-scale image revealing a regular patterning of the Pd(111) terraces resulting from the 2D oxide. The Fourier-transformed STM image [inset in (a)] reveals a rectangular lattice. (b) Tiling extracted from the atomic coordinates of (a). The characteristic repeating motif are rows of rhombuses in a dedicated sequence. The unit cell indicated by purple parallelograms consists of 40 atomic vertices forming 40 triangles, 15 squares, and five rhombuses [inset in (b)]. A domain boundary is running along the diagonal of the image. (a) $40 \times 40\,\text{nm}^2$, 0.5 nA, 1.0 V, $\Delta z = 125\,\text{pm}$.
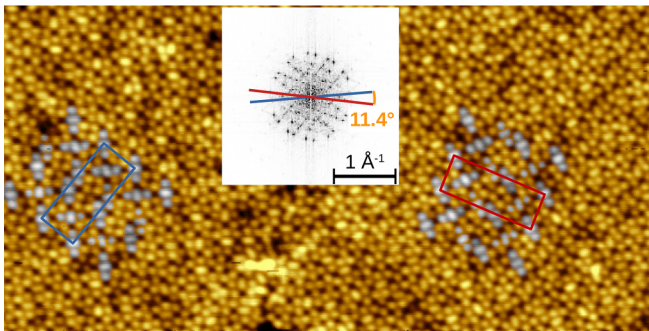
FIG. 4. STM image of two adjacent domains of the 40:15:5 approximant in Ba-Ti-O on Pd(111). The domains differ by rotation and are mirrored with respect to each other. From the FT image (inset) a spot splitting of 11.4° is determined for corresponding diffraction spots. $42 \times 21 \, \text{nm}^2$, 0.5 nA, 2 V, $\Delta z = 125 \, \text{pm}$.

Its triangle:square:rhombus tiling element ratio of 2.67:1:0.33 is identical to that of the 24:9:3 and 48:18:6 approximants observed for Sr-Ti-O on Pt(111) [2,5,15].

By mapping neighboring unit cells across the large-scale image, a one-dimensional domain boundary is obtained, which is filled by 60% of a full unit cell. In this region, only the double row of rhombuses exists and one single row is missing. This domain boundary is barely recognizable in the measured data in Fig. 3(a) since the tiling is continued without gaps or defects.

Figure 4 shows a domain boundary between two differently oriented domains of the **5R** approximant. In this case, a highly defective domain boundary is formed. For both domains three **5R** unit cells are indicated by highlighting their rhombuses. It turns out that the left domain is not only rotated with respect to the right one, but also mirrored. As a consequence, the FT image of the global STM image (inset in Fig. 4) reproduces the signature of the LEED data by having 12 pairs of spots at a scattering vector of about $1.0 \, \text{Å}^{-1}$. From the STM data a spot splitting of 11.4° is deduced for equivalent spots of both mirror domains.

FIG. 6. Comparison of the calculated (top) and measured (bottom) diffraction data for the **5R** approximant in Ba-Ti-O/Pd(111). The data compares a 180° radial cut through the reciprocal space as indicated in Fig. 2(b).

The experimental data have been used as input for modeling the diffraction pattern in a simple kinematic scattering theory approach. In a first step, the unit-cell basis has been modelled by distributing the Ba atoms according to the ideal tiling at a distance of 6.85 Å. In a second step, the unit-cell rotation of about 5.5° has been assumed and the pattern of all six rotational and mirror domains have been superimposed for comparison with the measured LEED pattern. When fine tuning the structural parameters, all attempts of finding a (higher-order) commensurate superstructure matrix failed. The measured diffraction pattern is reproduced best by assuming a $\begin{pmatrix} 26.45 & 10 \\ 1.03 & 9.8 \end{pmatrix}$ superstructure with respect to Pd(111). This matrix describes an oblique structure with a short unit-cell vector of 25.6 Å and a long one of 63.6 Å inclining a 92.5° angle. Figure 5 shows the calculated diffraction pattern of a single approximant domain. The most intense spots are observed close to the positions of the reciprocal lattice vectors of the dodecagonal quasicrystal observed for Ba-Ti-O on Pt(111) [3]. By superimposing the three rotational domains that exist for this oblique structure on the hexagonal substrate [Fig. 5(b)], these small local deviations from the ideal dodecagonal pattern result in a spot splitting in groups of three. Figure 5(c) properly aligns the overlay with the substrate and includes the three mirror domains of the approximant. Due to a rotation of the pattern with respect to the $\langle 1\bar{1}2 \rangle$ direction of
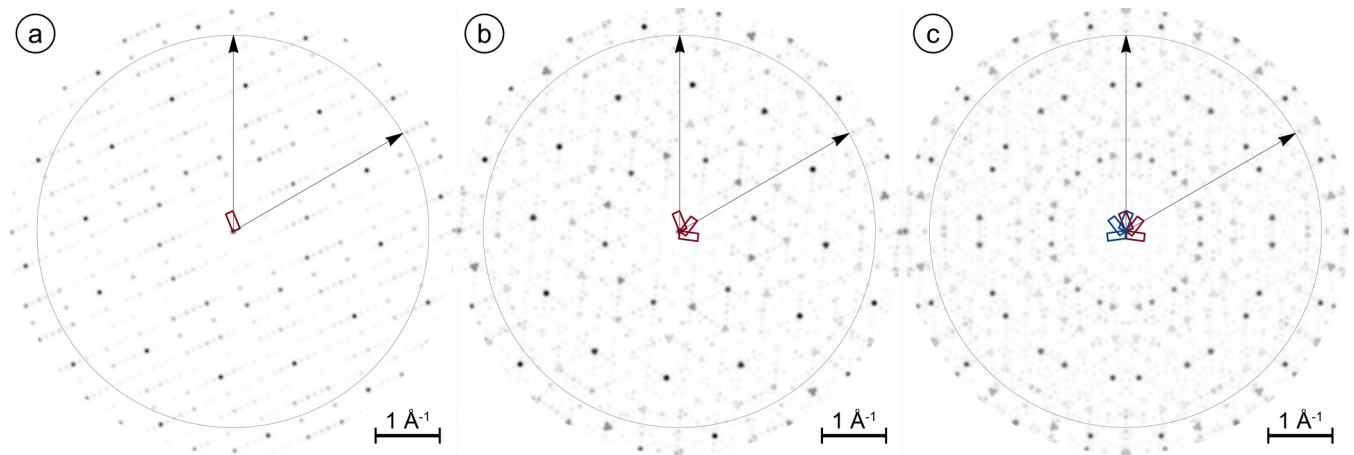

FIG. 5. Simulated diffraction pattern for the **5R** approximant structure in Ba-Ti-O/Pd(111). The black arrows and the circle indicate the reciprocal lattice of the substrate. (a) Single domain pattern with the reciprocal unit cell given in purple. (b) Superposition of the three rotational domains (purple), which is almost indistinguishable from a dodecagonal pattern. (c) The rotational alignment with respect to Pd(111) causes a spot doubling when including all mirror domains (blue).
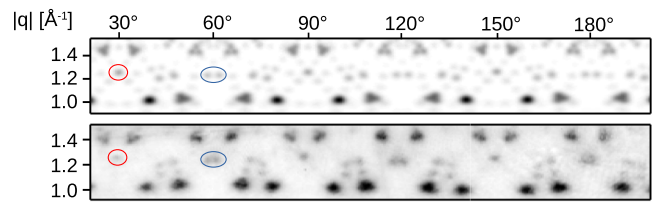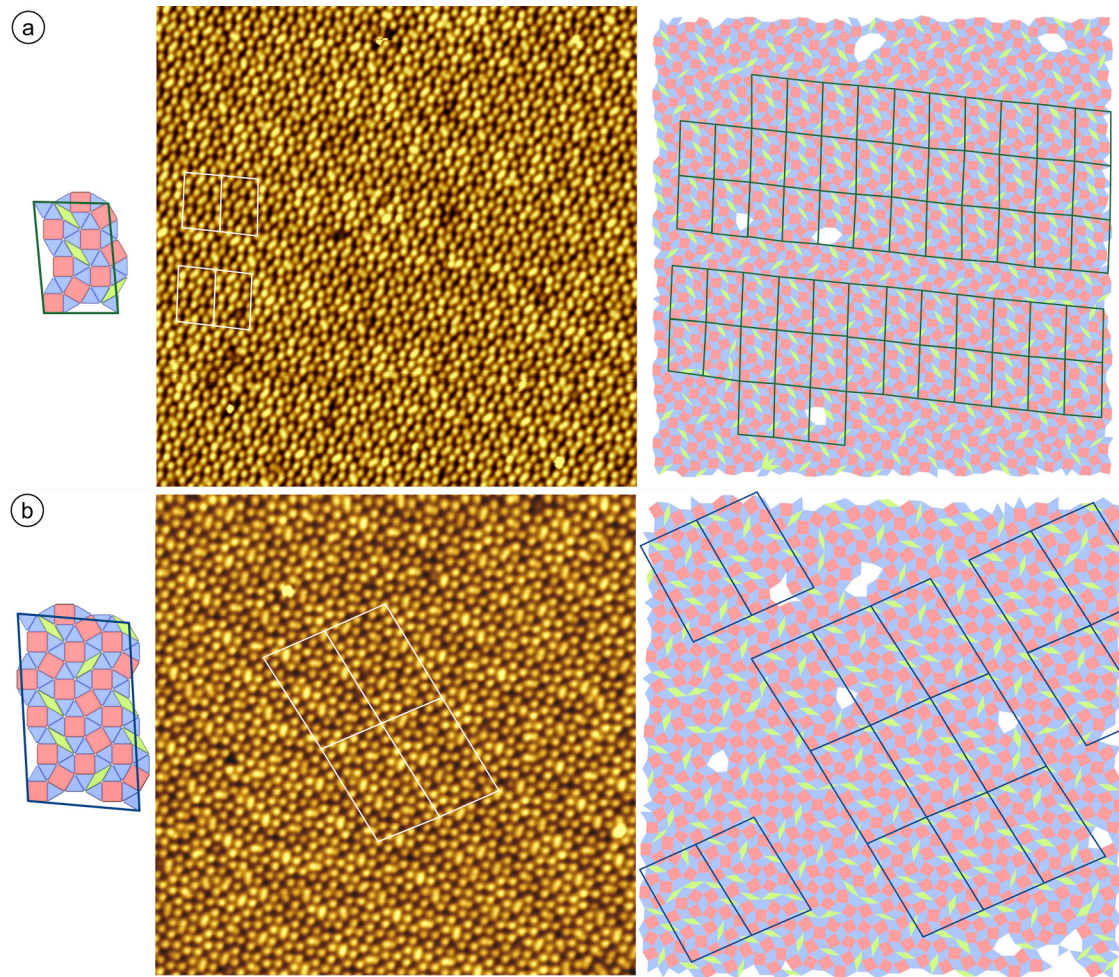
FIG. 7. Local modifications of the **5R** structure: (a) a **3R** approximant and (b) a **8R** approximant. The unit cells are shown next to the large-scale STM images and the tiling extracted from STM. Unit cells of the **3R** and the **8R** structure are highlighted in the tiling in green and blue, respectively. (a) $33 \times 33\,\mathrm{nm}^2$, 0.3 nA, 0.5 V, $\Delta z = 90$ pm, (b) $28.5 \times 28.5\,\mathrm{nm}^2$, 0.3 nA, -1.0 V, $\Delta z = 100$ pm.

Pd(111) a spot doubling occurs. The calculations confirm a rotation by $5.5\,^\circ$.

The good agreement that has been achieved by simulating the diffraction pattern of the approximant on the basis of the Ba atom positions is demonstrated by the comparison with the thick-line profile through the measured LEED data in Fig. 6. The detailed orientation and distance of the split spots at highest $|q|$ is the most sensitive measure for the validity of the unit vector aspect ratio and their orientation. The alternating occurrence of a single sharp spot and a pair of spots at $1.25\,\text{Å}^{-1}$ every $30\,^\circ$ is another proof (marked by red and blue circles). The only notable difference is the appearance of additional weak spots in direct neighborhood of the most intense spots at lowest $|q|$. These tiny differences might relate to the fact that only the subgrid of Ba atoms has been considered in the diffraction pattern calculations. The additional scatterer, namely the Ti and O atoms, representing $\sim \frac{7}{8}$ of all atoms in the unit cell have been neglected here. Utilizing the calculated unit cell dimensions, an average spacing of the Ba atoms of $(6.83 \pm 0.02)\,\text{Å}$ is obtained, which is in perfect agreement with that of the prototypical OQC in Ba-Ti-O/Pt(111). The OQC and the **5R** approximant share an Ba atom density of $2.46\,\mathrm{nm}^{-2}$.

Locally, two modifications of the sequence of rhombuses in the square-triangle-rhombus tilings are frequently observed. Figure 7(a) shows a large-area STM image of a region in which a smaller unit-cell structure is present. Its repeating unit contains 24 triangles, 9 squares, and three rhombuses [left in Fig. 7(a)] which is why this structure will be called **3R** approximant from now on. This approximant shares its short unit vector with the **5R** approximant. Moreover, its unit cell defines 60% of the unit cell of the **5R** approximant. The right part of Fig. 7(a) shows the full tiling extracted from the STM image. Two domains of the **3R** approximant can be identified, which are spanning the full width of the image, besides some local defects. The boundary separating the two domains is again a defect free continuation of the square-triangle-rhombus tiling, as seen for the **5R** approximant before. A different spot of the sample reveals a larger periodic approximant structure, which is shown in Fig. 7(b). In this structure, the unit cell is by roughly 50% larger as compared to the **5R** approximant and both structures have the long unit vector in common. Being built from 60 triangles, 22 squares, and eight rhombuses, it represents the largest approximant unit cell obtained in ternary oxide systems, so far. It contains a slightly smaller fraction of squares and an enlarged fraction
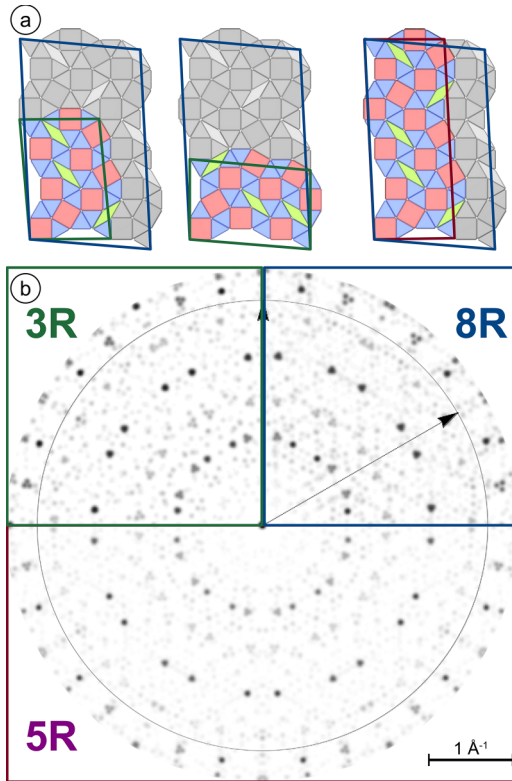
FIG. 8. (a) In the superposition of the **3R** (green) and **5R** (purple) unit cell tilings with that of the **8R** approximant (blue) a nesting of the three patches becomes visible. (b) Simulated diffraction pattern for the **3R** (upper left, green frame) and **8R** (upper right, blue frame) approximants in comparison to **5R** structure (bottom, purple frame).
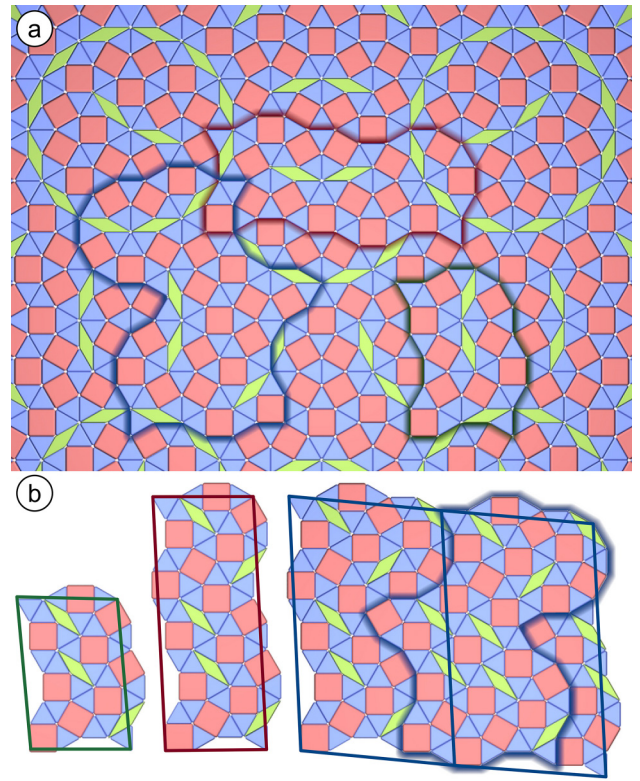

FIG. 9. (a) The outlines of the **3R**, **5R**, and **8R** approximants indicated in an ideal dodecagonal Niizeki-Gähler tiling. Within these outlines the number of tiling elements is identical. However, the basic tiles are differently arranged in the approximant unit cells given for comparison in (b). For the **8R** approximant, an alternative but valid motif has to be chosen as repeating unit cell in order to find a matching patch in the NGT.

of rhombuses, which is why its tiling element ratio changes to 2.73:1:0.36. As expected from its increasing complexity reflected in the large unit-cell size, the tiling element ratio is closest to that of the ideal OQC tiling of 2.73:1:0.37 [8]. This structure will be denoted **8R** structure. In the tiling extracted from the atomic positions in STM, an intact patch of 3×3 unit cells is found. More units exist in close vicinity disconnected by domain boundaries. Also units of **3R** and **5R** can be identified. By analyzing the Fourier-transformed STM images, all three approximants can be nicely distinguished as demonstrated in the Supplemental Material [20].

Figure 8(a) depicts the interesting relation between the **3R**, **5R**, and **8R** structures. They must be understood as being nested into each other. As shown on the left in Fig. 8(a), the **3R** unit cell (green) is identically found as a part of the **8R** structure (blue). In addition, both structures share one unit cell vector: The long unit cell vector of the **3R** structure is identical to the short one defining the **8R** unit cell. This is illustrated in the center of Fig. 8(a). In there, the **3R** patch is mirrored. In this configuration the tiling element distribution does not match that of the underlying **8R** structure, but the outline of the tiling patch is identical. Also the **5R** unit cell (purple) is part of the **8R** unit cell (blue) with a common long unit vector as shown on the right side of Fig. 8(a). Furthermore, the remaining area in the **8R** cell is again a complete patch out of the **5R**. By comparing the **3R** with the **5R** approximant it becomes obvious, that the **3R** unit cell tiling defines 60% of the **5R**

cell and both share the short unit vector. Knowing the exact unit-cell alignment to the substrate for the **5R** approximant, the above outlined equalities allow to simulate the diffraction pattern for the other two structures. Figure 8(b) shows a side-by-side comparison of the results obtained for the **3R** (left), the **8R** (right), and the **5R** (bottom) structure. Interestingly, despite large differences in the size of the reciprocal unit cells, all three pattern are hardly distinguishable. In an experimental LEED image the tiny differences regarding the spot splitting and spot densities will probably not be traceable.

IV. DISCUSSION

A. Relationship of approximants to the ideal dodecagonal square-triangle-rhombus tiling

On the tiling level, approximants are defined as periodic structure that repeats a patch of the parent quasicrystal (QC) tiling. For the presented **3R**, **5R**, and **8R** structures this requirement is not strictly fulfilled. For all three phases, the unit cell can be defined as a compact patch of the tiling whose outline is present in the OQC tiling. However, the sequence of tiles within this boundary is altered from the ideal OQC tiling. Figure 9(a) depicts a part of the dodecagonal Niizeki-Gähler tiling (NGT) with the boundaries of all three approximant phases indicated. Sharing these boundaries means that an
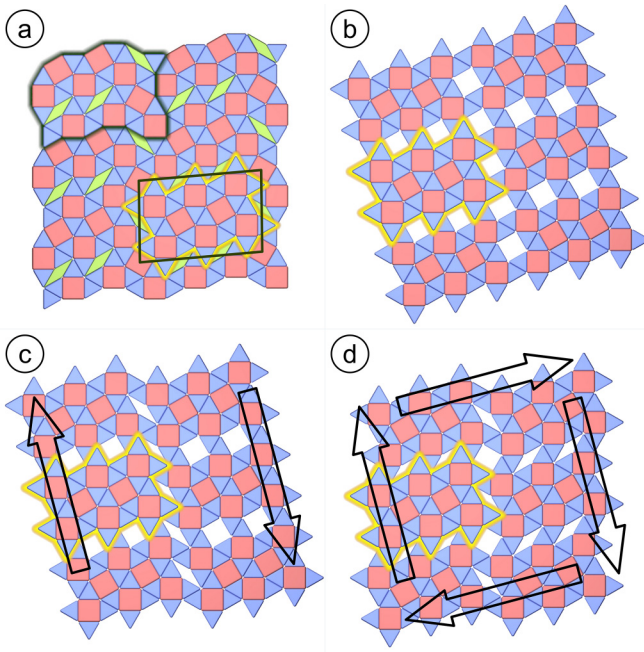
FIG. 10. (a) An alternative definition of the **3R** approximant unit cell with all rhombs at the edges. This way, a compact patch of the σ-phase approximant becomes prominently visible in the interior (black outline). (b) σ-phase tiling constructed by attaching six units outlined in black in (a). (c) By sliding neighboring units of (a) as indicated by the black arrows, a 1D antiphase domain boundary is formed, recognized by a line of rhombuses [16]. (d) Additional shifting in a perpendicular direction forms the **3R** approximant. Hence it can be interpreted as a ordered array of 2D antiphase domain boundaries in the σ phase.

identical number of the three basic tiles is contained in the patch. However, there is a major difference. In contrast to the approximants, the NGT does not contain individual rhombuses, but pairs of them. In order to rearrange the tiling inside the boundary into that of the approximants, phason flips must locally occur [21–25]. Phason flips are well-defined changes in the position of individual vertices resulting in a rearrangement of tiling elements. However, the tiling element frequencies stay constant upon phason flips. The evolution of the **3R** structure out of an ideal NGT patch is demonstrated in the Supplemental Material [20]. It is worth mentioning that despite the rearrangement of tiles in the approximant unit cells the local vertex configurations remain the same as found in the NGT.

B. Substrate rotation

To derive a deeper understanding of why **xR** approximants ($x = 3, 5, 8$) form, an alternative definition of the **3R** unit cell shown in Fig. 10(a) is chosen. In this definition, all rhombuses are aligned along the unit cell boundaries. Looking closely to the interior of this unit cell, a continuous patch of a simple square-triangle-tiling is seen. The respective patch is highlighted in yellow in Fig. 10(a). By periodic repetition of this patch and identifying the white remaining areas as squares as illustrated in Fig. 10(b) the well-known σ-phase approx-

imant is formed, which is extensively studied in 2D ternary oxides [10,12,14,16,26]. Recently, extended one-dimensional antiphase domain boundaries have been reported for the σ phase in Ba-Ti-O on Pd(111) that allow to accommodate an increased Ba vertex atom density [16]. Figure 10(c) illustrates how the vertical row of empty squares in the σ-phase patch of Fig. 10(b) is transformed into rhombuses by sliding neighboring patches along in the direction indicated by the black arrows. For the given patch this motion results in a reduction of the unit cell area by 4.5%. Hence, the vertex atom density per unit area is increased by this amount due to periodic repetition of these domain boundaries. Upon additional displacing of these patches also in the perpendicular direction, the **3R** approximant is created as illustrated in Fig. 10(d). The reduced number of empty squares in favor of an increasing amount of rhombuses immediately allows to recognize an additional increase of vertex atom density per unit area. In comparison to the σ phase, a ~9% higher vertex density is reached in the **3R** approximant. Based on Fig. 10, the **3R** approximant can be seen as the periodic repetition of antiphase domain boundaries in two dimensions. Similarly, the **5R** and **8R** approximants can be formed starting from a slightly different configuration of 1D domain boundaries (see Supplemental Material [20]). The vertex atom density in the **5R** approximant is identical to that of the **3R** approximant, which also follows from the identical tiling element ratio.

The identification of extended σ patches as the building block of the series of **xR** approximants underlines the importance of the σ phase for the epitaxial stabilization of the wealth of ternary oxide phases on hexagonal metal surfaces discussed previously [12].

C. Structural phase diagram for Ba-Ti-O/Pd(111)

So far, two-dimensional ternary oxide structures of Ba-Ti-O on Pd(111) were merely discussed on the tiling element level, in other words based on the Ba vertex atoms [16]. With the recent experimental confirmation of the tiling decoration scheme proposed by Cockayne *et al.* [4,5], a full atomistic picture of all phases can be presented. Figure 11 shows the structural phase diagram of 2D layers of Ba-Ti-O on Pd(111) in dependence of the Ba atom coverage per unit area. While the upper part reminds on the tiling, the lower part shows the Ba atoms residing on the vertex positions embedded in the network of Ti_nO_n network. The structure of lowest Ba atom density in Fig. 11 is the pure square-triangle tiling of the σ phase [16]. It consists of Ti_nO_n rings with $n = 4$ and 7. The ring occupation of 2/3 is directly reflected in the stoichiometry of $Ba_{0.67}Ti_2O_3$. In this kind of ternary oxide networks, Ba donates its valence electrons to the layer, which is why a dipole is associated to all Ba vertices [5,27]. The σ phase is the optimal solution to realize a common next-neighbor distance, which minimizes the electrostatic dipole-dipole repulsion between these Ba ions [5]. An increasing amount of Ba atoms results in an incorporation of rhombuses, and therefore $n = 10$ rings, into the tiling via one-dimensional antiphase domain boundaries. The additional oxygen atom in the $n = 10$ ring locally screens the charges of the nearby Ba ions, introducing a shorter vertex separation into the network,
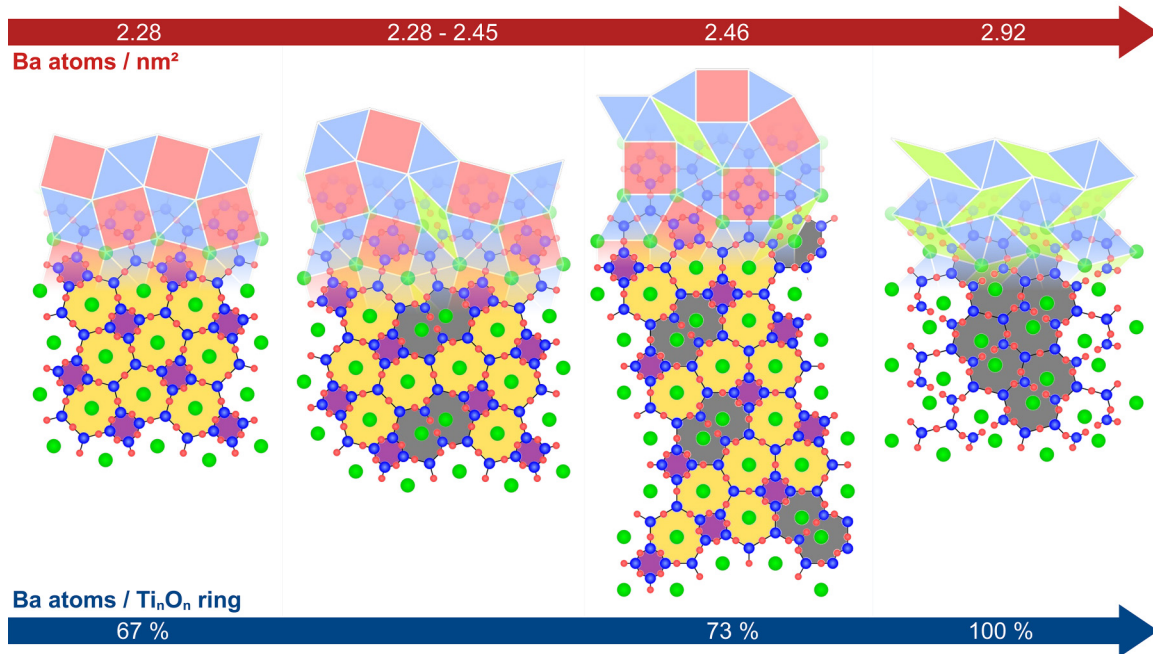
FIG. 11. Phase diagram of different long-range ordered structures for Ba-Ti-O on Pd(111) depending on their Ba density (top axis) and relative Ti_nO_n ring occupation (bottom axis). With increasing Ba density a transition from a square-triangle tiling (σ phase) via 1D and 2D antiphase domain boundaries (**5R** approximant) towards a triangle-rhombus tiling occurs. The different ring sizes of the Ti_nO_n network ($n = 4, 7, 10$) are color coded with $n = 4$ (purple), $n = 7$ (yellow), and $n = 10$ (grey).

which enables a higher packing density [5]. The frequency of the one dimensional rows of rhombuses is variable, thus Ba densities between 2.28 and 2.45 nm^{-2} can be realized [16]. However, at a Ba density of 2.46 nm^{-2}, respectively a stoichiometry of $Ba_{0.73}Ti_2O_{3.09}$, the series of **xR** approximants, as ordered arrays of 2D antiphase domain boundaries of σ-phase patches, is favoured against the 1D domain boundaries [28]. In terms of Ti_nO_n structure we find a combination of $n = 4, 7, 10$ rings. At 2.92 nm^{-2}, when all Ti_nO_n rings are occupied, a triangle-rhombus tiling emerges [16]. This structure is entirely formed from n = 10 rings (grey) occupied with two Ba atoms and one additional O atom. The **3R** and **5R** structures are found to have exactly the same Ba atom density of 2.46 nm^{-2} as the dodecagonal OQC, which is observed in the Ba-Ti-O system on Pt(111). The rotational degree of freedom of the ternary oxide on the Pd(111) support might be the reason for an epitaxial stabilization of σ-phase patches of different sizes as discussed before.

V. SUMMARY

We report on structure formation of Ba-Ti-O films on Pd(111) at the nominal composition of the dodecagonal OQC in Ba-Ti-O on Pt(111). Instead of aperiodic tilings, we find periodic structures, with triangle:square:rhombus tiling element ratios in their unit cells of 24:9:3, 40:15:5, and 60:22:8. Theses structures are rationalized as σ-phase patches incorporating antiphase domain boundaries in two orthogonal directions. A structural phase diagram for two-dimensional Ba-Ti-O on Pd(111) is presented for Ti_nO_n ring decorations with Ba atoms ranging from 67% to full coverage.

[1] S. Förster, K. Meinel, R. Hammer, M. Trautmann, and W. Widdra, Quasicrystalline structure formation in a classical crystalline thin-film system, Nature (London) **502**, 215 (2013).

[2] S. Schenk, S. Förster, K. Meinel, R. Hammer, B. Leibundgut, M. Paleschke, J. Pantzer, C. Dresler, F. O. Schumann, and W. Widdra, Observation of a dodecagonal oxide quasicrystal and its complex approximant in the SrTiO$_3$-Pt(111) system, J. Phys.: Condens. Matter **29**, 134002 (2017).

[3] E. M. Zollner, S. Schenk, M. Setvin, and S. Förster, Perfect monolayers of the BaTiO$_3$-derived 2D oxide quasicrystals investigated by scanning tunneling microscopy and noncontact atomic force microscopy, Phys. Status Solidi B **257**, 1900620 (2020).

[4] E. Cockayne, M. Mihalkovič, and C. L. Henley, Structure of periodic crystals and quasicrystals in ultrathin films of Ba-Ti-O, Phys. Rev. B **93**, 020101(R) (2016).

[5] S. Schenk, O. Krahn, E. Cockayne, H. L. Meyerheim, M. de Boissieu, S. Förster, and W. Widdra, 2D honeycomb transformation into dodecagonal quasicrystals driven by electrostatic forces, Nat. Commun. **13**, 7542 (2022).

[6] N. Niizeki and H. Mitani, Two-dimensional dodecagonal quasilattices, J. Phys. A: Math. Gen. **20**, L405 (1987).

[7] F. Gähler, *Quasicrystalline Materials* (World Scientific, Singapore, 1988)

[8] S. Schenk, E. M. Zollner, O. Krahn, B. Schreck, R. Hammer, S. Förster, and W. Widdra, Full real-space analysis of a dodecagonal quasicrystal, Acta Crystallogr. Sect. A **75**, 307 (2019).

[9] S. Förster, K. Meinel, K.-M. Schindler, and W. Widdra, Oxygen-deficient ordered phases of ultrathin $BaTiO_3$ films on Pt(111), Surf. Interface Anal. **44**, 628 (2012).

[10] S. Förster, M. Trautmann, S. Roy, W. A. Adeagbo, E. M. Zollner, R. Hammer, F. O. Schumann, K. Meinel, S. K. Nayak, K. Mohseni, W. Hergert, H. L. Meyerheim, and W. Widdra, Observation and Structure Determination of an Oxide Quasicrystal Approximant, Phys. Rev. Lett. **117**, 095501 (2016).

[11] S. Förster, S. Schenk, E. M. Zollner, O. Krahn, C.-T. Chiang, F. O. Schumann, A. Bayat, K.-M. Schindler, M. Trautmann, R. Hammer *et al.*, Quasicrystals and their approximants in 2D ternary oxides, Phys. Status Solidi B **257**, 1900624 (2020).

[12] E. M. Zollner, F. Schuster, K. Meinel, P. Stötzner, S. Schenk, B. Allner, S. Förster, and W. Widdra, Two-dimensional wetting layer structures of reduced ternary oxides on Ru(0001) and Pt(111), Phys. Status Solidi B **257**, 1900655 (2020).

[13] M. Maniraj, L. V. Tran, O. Krahn, S. Schenk, W. Widdra, and S. Förster, Hexagonal approximant of the dodecagonal oxide quasicrystal on Pt(111), Phys. Rev. Mater. **5**, 084006 (2021).

[14] T. T. Dorini, F. Brix, C. Chatelier, A. Kokalj, and É. Gaudry, Two-dimensional oxide quasicrystal approximants with tunable electronic and magnetic properties, Nanoscale **13**, 10771 (2021).

[15] C. R. Merchan, T. T. Dorini, F. Brix, L. Pasquier, M. Jullien, D. Pierre, S. Andrieu, K. Dumesnil, S. S. Parapari, S. Šturm *et al.*, Two-dimensional square and hexagonal oxide quasicrystal approximants in $SrTiO_3$ films grown on Pt(111)/Al_2O_3 (0001), Phys. Chem. Chem. Phys. **24**, 7253 (2022).

[16] F. E. Wührl, O. Krahn, S. Schenk, S. Förster, and W. Widdra, Antiphase domain boundary formation in 2D Ba-Ti-O on Pd(111): An alternative to phase separation, Phys. Status Solidi B **259**, 2100389 (2022).

[17] M. C. Militello and S. J. Simko, Elemental palladium by XPS, Surf. Sci. Spectra **3**, 387 (1994).

[18] M. H. Farstad, D. Ragazzon, H. Grönbeck, M. D. Strømsheim, C. Stavrakas, J. Gustafson, A. Sandell, and A. Borg, TiO_x thin films grown on Pd(100) and Pd(111) by chemical vapor deposition, Surf. Sci. **649**, 80 (2016).

[19] S. Förster, J. I. Flege, E. M. Zollner, F. O. Schumann, R. Hammer, A. Bayat, K.-M. Schindler, J. Falta, and W. Widdra, Growth and decay of a two-dimensional oxide quasicrystal: High-temperature in situ microscopy: Growth and decay of a two-dimensional oxide quasicrystal, Ann. Phys. **529**, 1600250 (2017).

[20] See Supplemental Material at http://link.aps.org/supplemental/10.1103/PhysRevB.107.195414 for (i) a comparison of the Fourier-transformed STM images of all three approximant phases; (ii) the sequence of phason flips transforming the 3R unit cell into that of the 24:9:3 approximant in Sr-Ti-O/Pt(111); and (iii) additional figures.

[21] R. Lück, Closeness condition and acceptance domains in chemically ordered quasilattices, Mater. Sci. Forum **150-151**, 145 (1994).

[22] H. Klein, M. Audier, M. Boudard, M. de Boissieu, L. Beraha, and M. Duneau, Phason defects in Al-Pd-Mn approximant phases, Philos. Mag. A **73**, 309 (1996).

[23] K. Edagawa, K. Suzuki, and S. Takeuchi, High Resolution Transmission Electron Microscopy Observation of Thermally Fluctuating Phasons in Decagonal Al-Cu-Co, Phys. Rev. Lett. **85**, 1674 (2000).

[24] C. L. Henley, M. de Boissieu, and W. Steurer, Discussion on clusters, phasons and quasicrystal stabilisation, Philos. Mag. **86**, 1131 (2006).

[25] M. Feuerbacher and M. Heggen, Metadislocations in complex metallic alloys and their relation to dislocations in Icosahedral quasicrystals, Isr. J. Chem. **51**, 1235 (2011).

[26] W. A. Adeagbo, I. V. Maznichenko, H. B. Hamed, I. Mertig, A. Ernst, and W. Hergert, Electronic and magnetic properties of $BaFeO_3$ on the Pt(111) surface in a quasicrystalline approximant structure, Phys. Status Solidi B **257**, 1900649 (2020).

[27] C. Wu, M. R. Castell, J. Goniakowski, and C. Noguera, Stoichiometry engineering of ternary oxide ultrathin films: $Ba_xTi_2O_3$ on Au(111), Phys. Rev. B **91**, 155424 (2015).

[28] Please note that the Ba density in the **8R** phase exceeds that of the **3R** and **5R** phases by 1%.